
Hephaestus Minicubes: A Global, Multi-Modal Dataset for Volcanic Unrest Monitoring

Nikolas Papadopoulos¹
npapadopoulos@mail.ntua.gr

Nikolaos Ioannis Bountos^{1,2}
bountos@noa.gr

Maria Sdraka^{1,2}
masdra@noa.gr

Andreas Karavias¹
andreas_karavias@mail.ntua.gr

Ioannis Papoutsis¹
ipapoutsis@mail.ntua.gr

¹ **Orion Lab**

National Observatory of Athens & National Technical University of Athens

² **Harokopio University of Athens**

Abstract

Ground deformation is regarded in volcanology as a key precursor signal preceding volcanic eruptions. Satellite-based Interferometric Synthetic Aperture Radar (InSAR) enables consistent, global-scale deformation tracking; however, deep learning methods remain largely unexplored in this domain, mainly due to the lack of a curated machine learning dataset. In this work, we build on the existing *Hephaestus* dataset, and introduce *Hephaestus Minicubes*, a global collection of 38 spatiotemporal datacubes offering high resolution, multi-source and multi-temporal information, covering 44 of the world’s most active volcanoes over a 7-year period. Each spatiotemporal datacube integrates InSAR products, topographic data, as well as atmospheric variables which are known to introduce signal delays that can mimic ground deformation in InSAR imagery. Furthermore, we provide expert annotations detailing the type, intensity and spatial extent of deformation events, along with rich text descriptions of the observed scenes. Finally, we present a comprehensive benchmark, demonstrating *Hephaestus Minicubes*’ ability to support volcanic unrest monitoring as a multi-modal, multi-temporal classification and semantic segmentation task, establishing strong baselines with state-of-the-art architectures. This work aims to advance machine learning research in volcanic monitoring, contributing to the growing integration of data-driven methods within Earth science applications.

1 Introduction

Ground deformation monitoring plays a vital role in volcanic hazard assessment, providing early insights into subsurface magmatic activity [Dzurisin, 2003]. It is widely regarded as one of the most reliable eruption precursors, with detectable signals that may emerge from days to even years before an event [Biggs et al., 2014]. Timely detection of such signals can offer critical lead time for risk mitigation and emergency response efforts [Tilling, 2008].

While ground-based networks, particularly those relying on Global Navigation Satellite Systems (GNSS), have traditionally been used to monitor deformation [Poland, 2024], many volcanoes

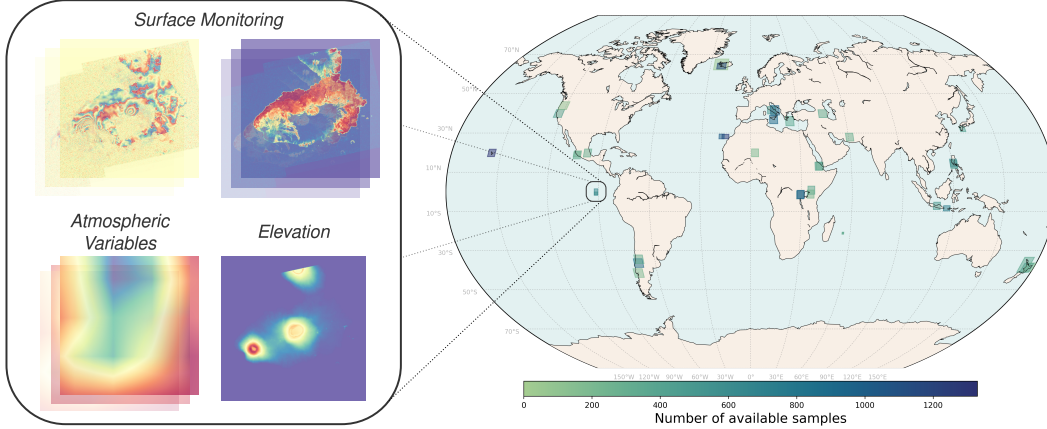


Figure 1: Hephaestus Minicubes data sources (left) vis-à-vis the spatial distribution of the minicubes (right). Box sizes on the map are proportional to frame dimensions and color intensity reflects the number of available products per region.

worldwide remain poorly instrumented or entirely unmonitored Loughlin et al. [2015]. This limitation, coupled with the growing availability of publicly accessible satellite data, from missions such as Copernicus Sentinel, has prompted a shift toward satellite-based approaches Spaans and Hooper [2016]. Among these, Interferometric Synthetic Aperture Radar (InSAR) has emerged as a powerful tool for global monitoring of surface motion [Hanssen, 2001].

InSAR estimates surface displacement with millimeter-level precision by analyzing phase differences between two or more SAR acquisitions from the same location at different times, while coherence quantifies the similarity between signals, serving as a measure of phase reliability and surface stability. A major challenge in interpreting InSAR data is distinguishing true ground deformation from atmospheric propagation delays. Lateral variations in ionospheric electron density and tropospheric water vapor concentration can alter the radar signal’s propagation time, introducing phase delays that contaminate the InSAR deformation signal [Zebker et al., 1997, Massonnet and Feigl, 1998, Beauducel et al., 2000]. These delays can produce artifacts that mimic real deformation, sometimes manifesting as apparent centimeter-scale ground motion [Doin et al., 2009], thereby complicating data interpretation and downstream analysis. The issue is even more prominent in volcanic regions, where complex atmospheric conditions—especially vertical stratification in mountainous terrain—can generate deformation-like patterns. This increases the risk of false positives in unrest detection, especially over elevated topography such as volcanoes and high-altitude ridges [Parker et al., 2015, Shirzaei and Bürgmann, 2012].

Deep learning pipelines have been successfully developed for various SAR-based tasks in Earth observation [Zhu et al., 2021], including natural disasters mapping (*e.g.* flood mapping Bountos et al. [2025]). However, their application to InSAR remains limited, mainly due to the lack of a curated machine learning dataset. This poses a significant barrier as the processing, understanding and annotation of InSAR products require specialized domain expertise. *Hephaestus* [Bountos et al., 2022c] marked the first attempt to construct a unique, expert-annotated InSAR dataset centered around volcanic activity monitoring. Despite its contributions, *Hephaestus* exhibits several limitations, which we discuss in detail in section 3.1, that have hindered its broader adoption within the community.

Our work builds on the *Hephaestus* dataset, by enhancing it both in ground sampling distance (GSD), as well as in information depth, by introducing additional data sources, and engineering its structure to better support time-series analysis. *Hephaestus Minicubes* introduces a collection of high-resolution spatiotemporal datacubes integrating InSAR phase difference and coherence products, digital elevation models (DEMs), and relevant atmospheric variables known to confound deformation signals (Fig. 1). In addition, we include a diverse set of expert annotations characterizing deformation type, intensity, and extent. Leveraging these improvements, we establish a comprehensive benchmark demonstrating the ability of *Hephaestus Minicubes* to support volcanic unrest monitoring as a multi-modal, multi-temporal classification and semantic segmentation task. We report strong baselines

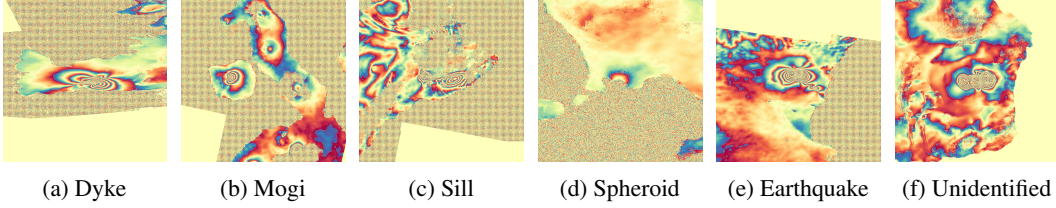


Figure 2: Examples of the different ground deformation types available in *Hephaestus Minicubes*.

using state-of-the-art architectures, while also identifying key limitations and challenges associated with applying deep learning in this context.

To support further research and promote the application of machine learning in InSAR-based volcanic unrest monitoring, we publicly release the *Hephaestus Minicubes* dataset at <https://github.com/Orion-AI-Lab/Hephaestus-minicubes>. The repository includes comprehensive documentation and is actively maintained to provide access to the latest version of the dataset. All code is released under the MIT License ¹ and data under the CC-BY license ².

2 Related Work

Despite the recent success of deep learning in Earth Observation (*e.g.* [Sumbul et al., 2021, Sdraka et al., 2024]), its adoption in the InSAR domain has remained limited. One of the main reasons for this is the lack of a large curated dataset, primarily due to a) the scarcity of positive instances and b) the high cost of the annotation process, which demands expert knowledge.

To overcome these challenges, and alleviate the need for time-consuming manual annotation, many works leveraged synthetically generated datasets, and models pretrained on optical tasks. In particular, [Anantrasirichai et al., 2018], relied on major data augmentations and transfer learning from ImageNet [Deng et al., 2009]. Building on this, several works focused on synthetically generated InSAR data to train Convolutional Neural Networks (CNNs) for ground deformation detection *e.g.* [Breneman and Barnhart, 2021, Anantrasirichai et al., 2019] and [Gaddes et al., 2024]. [Valade et al., 2019] utilized synthetic data to train a CNN to predict the associated phase gradients and phase decorrelation mask, which can later be used to detect ground displacement. Similarly, [Beker et al., 2023] utilized a synthetic dataset to train CNNs to detect subtle ground deformation from velocity maps. [Bountos et al., 2022a] proposed to train transformer architectures on synthetically generated InSAR using a prototype learning framework, assigning classes with a nearest-neighbor approach comparing the sample’s representation with the class prototypes.

Bountos et al. [2022b] diverged from this line of research and proposed the utilization of in-domain self-supervised contrastive learning to create reliable feature extractors without the need for human annotations, emphasizing the performance improvement compared to pretrained weights from optical tasks. In a separate line of work, [Popescu et al., 2024] proposed to formulate the volcanic ground deformation identification problem as an anomaly detection task utilizing Patch Distribution Modeling [Defard et al., 2021].

Given the gradual evolution of volcanic activity, time-series analysis is critical for effective monitoring, with several works exploring this direction. [Sun et al., 2020] trained a CNN on synthetic data, generated using the Mogi model as the deformation source. They created 20,000 time-series groups, with each group containing 20 time-consecutive pairs of unwrapped surface displacement maps. Moreover, [Ansari et al., 2021] proposed an unsupervised pipeline to cluster similar displacement patterns from InSAR time-series, building on a Long Short Term Memory (LSTM) autoencoder and Hierarchical Density-Based Spatial Clustering of Applications with Noise (HDBSCAN) Campello et al. [2013].

Finally, [Bountos et al., 2022c] introduced *Hephaestus* in an attempt to address the data scarcity at its core. *Hephaestus* was the largest manually annotated InSAR dataset to date with global coverage. Its introduction addressed many open gaps enabling the deployment of large deep learning models on a

¹<https://opensource.org/license/mit>

²<https://creativecommons.org/licenses/by/4.0/>

variety of ground deformation related problems, while paving the way for the adaptation of complex multi-modal tasks to the InSAR domain *e.g.* InSAR captioning and text to InSAR generation. Despite its significance, however, *Hephaestus* still presents notable limitations, which we discuss in detail in Section 3.1.

3 Dataset Construction

3.1 Building on Hephaestus

The *Hephaestus* dataset represents a significant step towards advancing machine learning-based approaches for volcanic unrest monitoring. While it offers rich, expert annotations across a global set of volcanoes, its effectiveness in high-precision and time-series geophysical analysis is limited by several factors. First, the spatial resolution of the annotated imagery is relatively coarse, at approximately $333\text{ m} \times 333\text{ m}$ per pixel. Second, the dataset consists of RGB composites of the InSAR products, lacking physically interpretable pixel values and geolocation information. Finally, the dataset structure is not designed for spatiotemporal modeling, lacking a machine-learning-friendly format. Recognizing both the promise and the limitations of *Hephaestus*, we take steps to redefine the dataset by addressing its weaknesses and expanding its scope.

3.2 Hephaestus Minicubes

In this work we introduce *Hephaestus Minicubes*, a collection of 38 datacubes covering 44 of the most active volcanoes globally from 2014 to 2021, with a significantly enhanced spatial resolution of approximately $100\text{ m} \times 100\text{ m}$ per pixel, containing a total of 19,942 annotated samples. Each datacube integrates InSAR products, topographic information, atmospheric variables that are known to introduce delays to SAR signals, combined under a diverse collection of expert annotations. The datacubes are stored in a compressed Zarr format [Miles et al., 2020], as structured multi-dimensional arrays optimized for efficient spatiotemporal analysis, with the full dataset totaling 1.7 TB.

In the following paragraphs, we provide a detailed description of each component of the *Hephaestus Minicubes* dataset, along with important design choices made during its development.

InSAR Products. The InSAR component lies at the core of the dataset, including: a) the wrapped *phase difference*, which captures surface displacement between SAR acquisitions, and b) the *coherence*, which measures the quality of the interferometric signal. These products are acquired by the COMET-LiCSAR system, which processes Copernicus Sentinel-1 imagery for global volcano surveillance, in a resolution of approximately $100\text{ m} \times 100\text{ m}$ per pixel. For more information on the InSAR generation and processing pipeline, readers are referred to [Lazecy et al., 2020].

Topography. Stratified atmospheric noise is often correlated with topography. To capture this we include the *Digital Elevation Model (DEM)* from LiCSAR, based on the 1 arc-second Shuttle Radar Topography Mission *DEM* [Farr et al., 2007]. This static variable is downsampled for each frame to match the resolution of the InSAR products, approximately $100\text{ m} \times 100\text{ m}$.

Atmospheric Component. A key advancement of *Hephaestus Minicubes* is the explicit integration of atmospheric variables known to directly contribute to phase delays in the SAR signal. These delays may produce patterns in InSAR imagery that closely resemble true surface deformation, [Zebker et al., 1997, Massonnet and Feigl, 1998, Beauducel et al., 2000] Following state-of-the-art atmospheric correction methods [Yu et al., 2018a] we incorporate atmospheric variables that represent humidity, temperature, and pressure. Specifically we include *Total Column Water Vapour*, *Surface Pressure*, and the *Vertical Integral of Temperature*, from the ERA5 single-level reanalysis dataset [Hersbach et al., 2020], for both primary and secondary SAR acquisition dates. We prioritize vertically integrated atmospheric measures, as the impact of atmospheric delays is not confined to specific atmospheric

Table 1: Summary of annotated activity variables

Annotation Variable	Count
Label	
Non-Deformation	18089
Deformation	1798
Earthquake	55
Activity Type	
Sill	1258
Dyke	527
Mogi	333
Earthquake	55
Unidentified	50
Spheroid	25
Intensity Level	
Low	908
Medium	533
High	751
None	55
Phase	
Rest	18089
Unrest	1664
Rebound	134
None	15

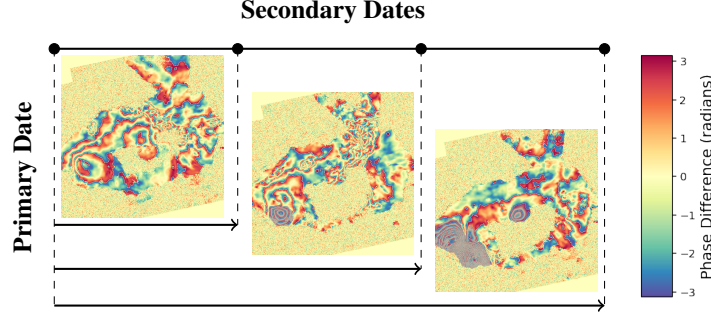


Figure 3: Schematic representation of the time-series construction method. A single primary acquisition date is associated with multiple secondary dates, forming a sequence of InSAR products. Each image displays the phase difference with an overlaid mask to highlight areas with apparent deformation.

layers. We select the ERA5 data closest in time to each SAR acquisition and resample them to align with the spatial resolution of the InSAR data.

Expert Annotations. *Hephaestus Minicubes* builds upon the manually curated annotations provided by *Hephaestus*, adapting them to the datacube format by converting relevant labels into spatiotemporal masks and carefully addressing differences in spatial resolution and alignment. The available spatiotemporal masks include multi-level information on *ground deformation*, *activity type* (e.g. Dyke, Sill, Spheroid, etc.), and *intensity level* (e.g. Low, Medium, High), while the related volcano’s *phase* (e.g. Rest, Unrest, Rebound) is represented as a categorical variable (see Tab.1). Additional annotations provide auxiliary information on the presence and type of noise, quality of the samples, annotator confidence and a textual description, offering expert commentary and annotation rationale. Detailed information on all available labels is provided in the Supplemental Material.

4 Benchmark

To enable a fair comparison of future methods for InSAR based volcanic unrest detection, we provide the first benchmark on *Hephaestus Minicubes*. This benchmark is designed to serve as a strong baseline across two fundamental tasks: binary ground deformation classification and semantic segmentation. To transform our problem to a binary task, we group all sub-classes of ground deformation (e.g. Mogi, Sill) into one class. Below we present the main decisions made for the experimental setup. For detailed information on the complete experimental framework, readers are referred to the Supplemental Material.

Data Split. We apply a temporal data split, separating InSAR products by the primary acquisition date. The training set includes interferograms with the primary SAR acquired between January 1, 2014, and May 31, 2019, while the validation from June 1, 2019, to December 31, 2019. Finally the test set consists of interferograms with primary acquisition dates between January 1, 2020, and December 31, 2021. This split was carefully chosen to maintain spatial diversity by including data from all the available frames, with an adequate ratio of positive samples in each set, as seen in Tab. 2.

Data Preparation. To reduce input size, each InSAR product is cropped to 512×512 pixels. We apply cropping with a random offset from the frame center, ensuring any existing deformation patterns are included within the cropped area. We address class imbalance, by undersampling during training, using all available positive samples and an equal number of random negative samples in each epoch, and apply data augmentation to improve model generalization.

Constructing InSAR Time-Series. Constructing meaningful InSAR time-series is non-trivial due to the bi-temporal nature of each product, characterized by both primary and secondary acquisition dates. Moreover, the temporal gap between the primary and secondary acquisition in *Hephaestus* is not fixed, making temporal ordering highly ambiguous. In our framework, we define a valid time series as a sequence of interferograms that share the same primary and different secondary acquisition

Table 2: Summary of the temporal split windows and class distribution for both the single-timestep and time-series approaches.

Split	Dates	Single-Timestep		Time-Series	
		Positives	Negatives	Positives	Negatives
Training	Jan 2014 – May 2019	1143	8697	701	2626
Validation	Jun 2019 – Dec 2019	154	2416	75	728
Test	Jan 2020 – Dec 2021	509	5992	225	1776
Sum	Jan 2014 – Dec 2021	1806	17105	1001	5130

dates. These sequences are then ordered chronologically based on the secondary dates, as illustrated in Fig. 3.

This formulation allows models to observe the evolution of deformation relative to a fixed reference, providing insights into the dynamics of volcanic unrest. At the same time, sampling different secondary acquisitions can expose the model to variations in atmospheric noise, thereby encouraging learning of more robust, discriminative features [Dzurisin, 2003].

The number of valid InSAR products per primary SAR acquisition date varies across the dataset. To maintain a consistent input shape for model training, we either select all subsets that match the target sequence length or apply controlled duplication of available products when necessary. After examining the distribution of available secondary dates for each primary date, we choose to construct *time-series of length 3*, aiming for a balance between a rich temporal sequence and limited duplications.

In the time-series setting, labels are aggregated across the sequence. For the classification task, a sequence is considered positive if at least one of the products is labeled as showing deformation. For the segmentation task, the target mask is defined as the union of all individual deformation masks across the sequence. This approach ensures that models can leverage temporal information while maintaining a single target.

Models. We employ a diverse set of state-of-the-art models, widely used in Earth observation benchmarks (*e.g.* GEO-Bench Lacoste et al. [2023]), assessing their capacity for ground deformation classification and segmentation. For the classification task, we include ResNet-50 [He et al., 2016], Vision Transformer (ViT) [Dosovitskiy et al., 2020], ConvNeXt [Liu et al., 2022], MobileNetV3 [Howard et al., 2019], and EfficientNetV2 [Tan and Le, 2021], all pretrained on ImageNet [Deng et al., 2009]. For the segmentation task, we use UNet [Ronneberger et al., 2015], DeepLabv3 [Chen et al., 2017] and SegFormer [Xie et al., 2021], with ResNet-50 backbones pretrained on ImageNet.

Evaluating Input Contributions. Exploiting the diverse information of *Hephaestus Minicubes*, we examine the models’ performance across varying configurations to evaluate the importance of each available data source. We vary the input on two dimensions for both classification and segmentation tasks. First, we examine the significance of temporal context in detecting volcanic unrest on both single-timestep and time-series setups. Second, we assess the impact of the auxiliary atmospheric variables by evaluating the models’ performance with and without them. In Tabs. 3 and 4, we present the classification and segmentation results, respectively, reporting Precision, Recall, F1-score, and Area Under the Receiver Operating Characteristic curve (AUROC) for the classification task, and Precision, Recall, F1-score, and Intersection over Union (IoU) for the segmentation task. To account for variability introduced by initialization, undersampling, and augmentations, we report the average performance along with standard deviation over three random seeds.

5 Discussion

Overall performance. Examining the performance of the classification baselines in Tab. 3, we observe strong discriminative capability reaching up to $\approx 79\%$ in F1-Score. However, this performance declines in the segmentation task reaching up to $\approx 71\%$. This is not a surprising behavior, as exact delineation of ground deformation is often non-trivial even for experts. Even after discerning true ground deformation fringes from atmospheric contributions, defining the extent of such fringes is an ambiguous process, especially in regions with high incoherence. Such noise is inherent to the data

Table 3: Deformation classification metrics (mean \pm std) for best model configurations between different random seeds. The tables report Precision (Prec), Recall (Rec), F1-score (F1), and Area Under the Receiver Operating Characteristic curve (AUROC) for the deformation class. The best value in each column is marked in **bold**, and the second best is underlined.

	Model	Atm.	Prec	Rec	F1	AUROC
Single-Timestep	ResNet-50	\times	83.63 \pm 2.94	68.5 \pm 3.05	75.29 \pm 2.74	96.99 \pm 0.39
		\checkmark	87.53 \pm 3.7	64.37 \pm 1.64	74.18 \pm 2.32	<u>96.26</u> \pm 0.88
	MobileNetV3	\times	95.03 \pm 1.17	64.77 \pm 0.88	77.02 \pm 0.37	92.06 \pm 2.61
		\checkmark	89.56 \pm 0.54	<u>69.02</u> \pm 1.79	78.06 \pm 1.13	91.99 \pm 2.32
	EfficientNetV2	\times	76.28 \pm 3.74	44.66 \pm 2.71	56.18 \pm 1.08	74.98 \pm 4.13
		\checkmark	82.28 \pm 3.55	49.44 \pm 4.22	61.61 \pm 3.1	83.25 \pm 5.02
	ConvNeXt	\times	93.04 \pm 1.85	69.09 \pm 2.01	<u>79.25</u> \pm 0.69	90.01 \pm 3.88
		\checkmark	<u>93.58</u> \pm 0.3	68.76 \pm 1.89	79.26 \pm 1.33	90.29 \pm 1.75
	ViT	\times	85.16 \pm 11.21	55.8 \pm 10.03	67.3 \pm 10.51	87.58 \pm 5.02
		\checkmark	90.75 \pm 1.51	59.27 \pm 7.47	71.45 \pm 5.45	88.6 \pm 3.0
Time-Series	ResNet-50	\times	67.79 \pm 2.11	60.0 \pm 0.36	63.64 \pm 0.89	92.68 \pm 1.84
		\checkmark	68.65 \pm 0.85	59.41 \pm 3.27	63.66 \pm 2.08	88.0 \pm 2.33
	MobileNetV3	\times	64.08 \pm 1.38	63.56 \pm 3.82	63.79 \pm 2.54	89.39 \pm 1.16
		\checkmark	63.51 \pm 4.46	<u>65.48</u> \pm 5.88	64.29 \pm 3.71	89.29 \pm 1.06
	EfficientNetV2	\times	68.58 \pm 2.94	49.04 \pm 7.26	56.88 \pm 5.36	82.22 \pm 3.5
		\checkmark	64.23 \pm 9.07	56.0 \pm 2.97	59.42 \pm 4.2	82.63 \pm 1.54
	ConvNeXt	\times	73.19 \pm 2.02	68.89 \pm 15.12	70.36 \pm 8.63	91.65 \pm 5.01
		\checkmark	<u>75.88</u> \pm 7.14	57.48 \pm 2.55	65.36 \pm 4.3	78.24 \pm 3.18
	ViT	\times	80.52 \pm 5.61	53.48 \pm 4.62	63.92 \pm 1.69	91.21 \pm 3.26
		\checkmark	71.19 \pm 2.74	61.63 \pm 13.4	<u>65.54</u> \pm 8.5	89.2 \pm 3.42

Table 4: Deformation segmentation metrics (mean \pm std) for best model configurations between different random seeds. The tables report Precision (Prec), Recall (Rec), F1-score (F1), and Intersection over Union (IoU) for the deformation class. The best value in each column is marked in **bold**, and the second best is underlined.

	Model	Atm.	Prec	Rec	F1	IoU
Single-Timestep	DeepLabv3	\times	81.41 \pm 1.42	63.74 \pm 0.52	71.49 \pm 0.30	55.63 \pm 0.37
		\checkmark	81.64 \pm 1.77	60.82 \pm 2.61	69.65 \pm 1.48	53.46 \pm 1.75
	UNet	\times	<u>82.43</u> \pm 0.64	61.25 \pm 1.27	<u>70.27</u> \pm 0.63	<u>54.17</u> \pm 0.75
		\checkmark	81.70 \pm 0.41	53.71 \pm 1.89	64.80 \pm 1.48	47.95 \pm 1.62
	SegFormer	\times	80.87 \pm 1.74	<u>61.32</u> \pm 1.96	69.70 \pm 0.70	53.50 \pm 0.82
		\checkmark	83.13 \pm 2.30	55.71 \pm 0.98	66.68 \pm 0.22	50.01 \pm 0.25
Time-Series	DeepLabv3	\times	<u>75.68</u> \pm 2.15	54.66 \pm 1.54	63.42 \pm 0.25	46.44 \pm 0.27
		\checkmark	74.64 \pm 2.48	46.67 \pm 2.15	57.39 \pm 1.84	40.27 \pm 1.82
	UNet	\times	74.57 \pm 3.10	58.57 \pm 2.39	<u>65.50</u> \pm 0.35	<u>48.7</u> \pm 0.39
		\checkmark	70.28 \pm 4.56	44.18 \pm 1.64	54.19 \pm 2.03	37.2 \pm 1.92
	SegFormer	\times	79.22 \pm 0.55	<u>57.87</u> \pm 1.46	66.87 \pm 0.77	50.23 \pm 0.87
		\checkmark	<u>77.14</u> \pm 0.10	47.88 \pm 2.73	59.05 \pm 2.10	41.92 \pm 2.12

itself, making the annotation, and thereby accurate prediction challenging Kondylatos et al. [2025]. Many works have sought to improve segmentation capabilities in such conditions *e.g.* Acuna et al. [2019], Yu et al. [2018b]. Our benchmark establishes a strong reference point for future methods aimed at addressing these complexities.

Impact of temporal dimension. Examining both classification and segmentation experiments, we note a surprising drop in performance when we use a time-series input. While the theoretical advantages of using time-series data to capture volcanic unrest and account for atmospheric delays

are well established [Dzurisin, 2003], it is important to note that performance comparisons between single-timestep and time-series inputs are not entirely equivalent in our framework. Although both approaches aim to detect the same underlying geophysical phenomena, they operate on different data subsets due to the stricter requirements for constructing valid time-series (See Tab. 2). More importantly, the task formulation shifts: single-timestep models predict deformation masks for individual images, while time-series models segment the union of deformation patterns across multiple observations, effectively capturing the total extent of the affected area. As such, while performance trends are informative, variability in absolute metrics between the two setups should be interpreted with these structural differences in mind.

Impact of atmospheric variables. The impact of atmospheric information varies across tasks. In classification, some models exhibit modest performance gains with the inclusion of atmospheric context, with EfficientNetV2 and ViT demonstrating a consistent improvement both in the single-timestep and the time-series settings. In contrast, atmospheric information does not lead to improved performance in segmentation models. This discrepancy likely reflects the different demands of the two tasks. While atmospheric variables offer valuable insights into the atmospheric conditions, they are available at a substantially coarser spatial resolution than the InSAR data itself. This resolution mismatch may constrain their effectiveness, particularly in segmentation tasks where fine-grained spatial detail is critical for distinguishing true deformation from confounding patterns. Moreover, InSAR data offer significantly stronger information for the detailed delineation of ground deformation, which may lead it to dominate the learning process diminishing the influence of atmospheric input.

Motivated by this discussion, we examine specific cases where the inclusion of atmospheric variables helps the model mitigate false positives caused by atmospheric delays in semantic segmentation. In doing so, we aim to explore potential nuances that are not fully captured by aggregate performance metrics, in order to better understand the limitations of our baseline modeling approach and identify possible paths forward. In Fig. 4 we compare predicted masks from models trained with and without atmospheric inputs. Along with this, we also investigate the mean lateral gradient of total column water vapour (TCWV) across the primary and secondary SAR acquisition dates, contextualized against the broader distribution of mean TCWV gradients for the given frame, as lateral variation in atmospheric moisture is a key driver of atmospheric phase delays in InSAR measurements. Notably, both scenes exhibit high lateral variation in TCWV, suggesting that the atmospheric component can, under specific conditions, contribute meaningful information about phase delay artifacts. However, incorporating this knowledge into deep learning models remains a non-trivial challenge, particularly due to the aforementioned mismatch in resolution and information density between atmospheric inputs and InSAR data.

Finally, the inclusion of the atmospheric component as additional channels, for both primary and secondary SAR acquisitions, comes with a significant increase in input dimensionality, thereby adding to model complexity and potentially hindering performance. Effective and efficient handling of the atmospheric component remains a non-trivial and open challenge. Addressing this issue may require more sophisticated and context-aware approaches that model both the internal relationships of the atmospheric variables, as well as cross-modal interactions with the InSAR imagery.

5.1 Limitations

Despite extensive efforts in the annotation process, which incorporates validation from both internal and external sources, annotating InSAR imagery remains inherently challenging. The labels used for training and evaluation are not free from noise, reflecting the complexities involved in detecting volcanic unrest. The subtlety and variability of volcanic deformation patterns often lead to ambiguities in interpretation, making accurate and consistent annotation difficult, especially in regions with low signal coherence. This limitation is compounded by the fact that some volcanic events are subtle or evolve over extended periods, which can further complicate the identification and classification of deformation signals in the data.

Additionally, the temporal scale and nature of volcanic activity introduce significant challenges. Some unrest episodes are subtle and unfold over many years, while others are abrupt and short-lived. The frequency and expression of these events vary widely between volcanoes; some may remain inactive for extended periods before suddenly exhibiting signs of unrest. Consequently, certain volcanoes may not show any positive samples during the dataset’s timeframe, limiting the model’s exposure to their activity patterns. As a result, models trained under such constraints may struggle to generalize

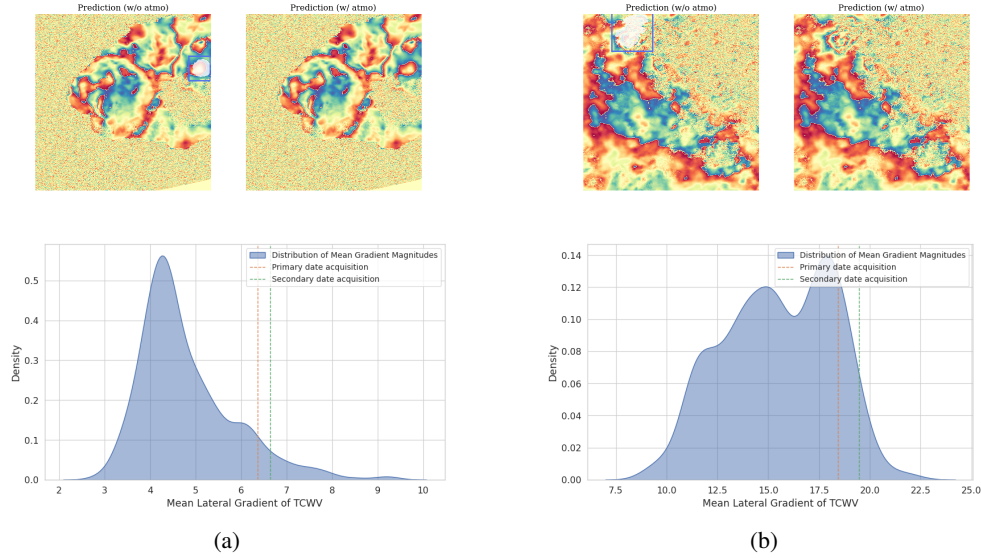


Figure 4: Compact view of DeepLabV3 predictions (top) with and without atmospheric input and the associated mean lateral gradient distributions of TCWV (bottom) for two samples: (a) Sierra Negra volcano, Galápagos islands. (15/3/2020 - 15/04/2020), (b) Valle de Piedras Encimadas region in Puebla, Mexico (05-08-2020 - 17/08/2020). We examine, representative examples where the inclusion of atmospheric variables leads to improved segmentation performance by mitigating false positives linked to atmospheric artifacts. In both cases, this improvement coincides with high lateral variation in TCWV, hinting at the potential value of atmospheric variables.

effectively in operational settings, particularly when tasked with detecting unrest at volcanoes with sparse or no prior positive observations.

6 Conclusion

Hephaestus Minicubes represents a significant advancement in data-driven volcanic unrest monitoring. By integrating high-resolution InSAR phase and coherence products, digital elevation models, atmospheric information and expert annotations into structured spatiotemporal datacubes, the dataset provides a rich foundation for machine learning research in this domain. The additional inclusion of atmospheric variables addresses a key challenge in InSAR analysis—distinguishing true ground deformation from atmospheric phase delays that can mimic similar patterns.

Building on *Hephaestus Minicubes*, we provide an extensive benchmark demonstrating the dataset’s ability to support volcanic unrest monitoring as a multi-modal, multi-temporal problem. We examine two fundamental tasks, *i.e.* InSAR classification and semantic segmentation, across both single-timestep and time-series formats. Our results establish strong baselines for future applications, assessing the capacity of state-of-the-art architectures in this domain. The inclusion of time-series and atmospheric data—while theoretically promising—reveals practical complexities. Similarly, while atmospheric variables can help mitigate false positives from phase delay artifacts, their coarse spatial resolution and increased model complexity limit their overall utility in segmentation tasks. These findings underscore the importance of developing more nuanced, context-aware modeling strategies that can effectively leverage atmospheric information and temporal context, pointing to promising directions for future research.

Hephaestus Minicubes is, to the best of our knowledge, the first large-scale machine learning ready dataset to incorporate such diverse information. We believe *Hephaestus Minicubes* will be a valuable asset to the research community, contributing to the growing integration of data-driven methods within Earth science applications.

Acknowledgments and Disclosure of Funding

This work has received funding from the project ThinkingEarth (grant agreement No 101130544) of the European Union’s Horizon Europe research and innovation programme.

References

- David Acuna, Amlan Kar, and Sanja Fidler. Devil is in the edges: Learning semantic boundaries from noisy annotations. In *Proceedings of the IEEE/CVF conference on computer vision and pattern recognition*, pages 11075–11083, 2019.
- N. Anantrasirichai, J. Biggs, F. Albino, P. Hill, and D. Bull. Application of Machine Learning to Classification of Volcanic Deformation in Routinely Generated InSAR Data. *Journal of Geophysical Research: Solid Earth*, 123(8):6592–6606, August 2018. ISSN 2169-9313, 2169-9356. doi: 10.1029/2018JB015911. URL <https://agupubs.onlinelibrary.wiley.com/doi/10.1029/2018JB015911>.
- Nantheera Anantrasirichai, Juliet Biggs, Fabien Albino, and David Bull. A deep learning approach to detecting volcano deformation from satellite imagery using synthetic datasets. *Remote Sensing of Environment*, 230: 111179, 2019.
- Homa Ansari, Marc Rußwurm, Mohsin Ali, Sina Montazeri, Alessandro Parizzi, and Xiao Xiang Zhu. Insar displacement time series mining: A machine learning approach. In *2021 IEEE International Geoscience and Remote Sensing Symposium IGARSS*, pages 3301–3304. IEEE, 2021.
- François Beauducel, Pierre Briole, and Jean-Luc Froger. Volcano-wide fringes in ers synthetic aperture radar interferograms of etna (1992–1998): Deformation or tropospheric effect? *Journal of Geophysical Research: Solid Earth*, 105(B7):16391–16402, 2000.
- Teo Beker, Homa Ansari, Sina Montazeri, Qian Song, and Xiao Xiang Zhu. Deep learning for subtle volcanic deformation detection with insar data in central volcanic zone. *IEEE Transactions on Geoscience and Remote Sensing*, 61:1–20, 2023.
- J Biggs, SK Ebmeier, WP Aspinall, Z Lu, ME Pritchard, RSJ Sparks, and TA Mather. Global link between deformation and volcanic eruption quantified by satellite imagery. *Nature communications*, 5(1):1–7, 2014.
- Nikolaos Ioannis Bountos, Dimitrios Michail, and Ioannis Papoutsis. Learning from synthetic insar with vision transformers: The case of volcanic unrest detection. *IEEE Transactions on Geoscience and Remote Sensing*, 60:1–12, 2022a.
- Nikolaos Ioannis Bountos, Ioannis Papoutsis, Dimitrios Michail, and Nantheera Anantrasirichai. Self-Supervised Contrastive Learning for Volcanic Unrest Detection. *IEEE Geoscience and Remote Sensing Letters*, 19:1–5, 2022b. ISSN 1545-598X, 1558-0571. doi: 10.1109/LGRS.2021.3104506. URL <https://ieeexplore.ieee.org/document/9517282/>.
- Nikolaos Ioannis Bountos, Ioannis Papoutsis, Dimitrios Michail, Andreas Karavias, Panagiotis Elias, and Isaak Parcharidis. Hephaestus: A Large Scale Multitask Dataset Towards InSAR Understanding. In *Proceedings of the IEEE/CVF Conference on Computer Vision and Pattern Recognition (CVPR) Workshops*, pages 1453–1462, June 2022c.
- Nikolaos Ioannis Bountos, Maria Sdraka, Angelos Zavras, Andreas Karavias, Ilektra Karasante, Themistocles Herekakis, Angeliki Thanasou, Dimitrios Michail, and Ioannis Papoutsis. Kuro siwo: 33 billion m² under the water. a global multi-temporal satellite dataset for rapid flood mapping. *Advances in Neural Information Processing Systems*, 37:38105–38121, 2025.
- Clayton MJ Brengman and William D Barnhart. Identification of surface deformation in insar using machine learning. *Geochemistry, Geophysics, Geosystems*, 22(3):e2020GC009204, 2021.
- Ricardo JGB Campello, Davoud Moulavi, and Jörg Sander. Density-based clustering based on hierarchical density estimates. In *Pacific-Asia conference on knowledge discovery and data mining*, pages 160–172. Springer, 2013.
- Liang-Chieh Chen, George Papandreou, Florian Schroff, and Hartwig Adam. Rethinking atrous convolution for semantic image segmentation. *arXiv preprint arXiv:1706.05587*, 2017.
- Thomas Defard, Aleksandr Setkov, Angelique Loesch, and Romaric Audigier. Padim: a patch distribution modeling framework for anomaly detection and localization. In *International conference on pattern recognition*, pages 475–489. Springer, 2021.

- Jia Deng, Wei Dong, Richard Socher, Li-Jia Li, Kai Li, and Li Fei-Fei. Imagenet: A large-scale hierarchical image database. In *2009 IEEE conference on computer vision and pattern recognition*, pages 248–255. Ieee, 2009.
- M-P Doin, Cécile Lasserre, Gilles Peltzer, Olivier Cavalié, and Cécile Doubre. Corrections of stratified tropospheric delays in sar interferometry: Validation with global atmospheric models. *Journal of Applied Geophysics*, 69(1):35–50, 2009.
- Alexey Dosovitskiy, Lucas Beyer, Alexander Kolesnikov, Dirk Weissenborn, Xiaohua Zhai, Thomas Unterthiner, Mostafa Dehghani, Matthias Minderer, Georg Heigold, Sylvain Gelly, et al. An image is worth 16x16 words: Transformers for image recognition at scale. *arXiv preprint arXiv:2010.11929*, 2020.
- Daniel Dzurisin. A comprehensive approach to monitoring volcano deformation as a window on the eruption cycle. *Reviews of Geophysics*, 41(1), 2003. doi: <https://doi.org/10.1029/2001RG000107>. URL <https://agupubs.onlinelibrary.wiley.com/doi/abs/10.1029/2001RG000107>.
- Tom G Farr, Paul A Rosen, Edward Caro, Robert Crippen, Riley Duren, Scott Hensley, Michael Kobrick, Mimi Paller, Ernesto Rodriguez, Ladislav Roth, et al. The shuttle radar topography mission. *Reviews of geophysics*, 45(2), 2007.
- Yuri Fialko, Yakov Khazan, and Mark Simons. Deformation due to a pressurized horizontal circular crack in an elastic half-space, with applications to volcano geodesy. *Geophysical Journal International*, 146(1):181–190, 2001.
- M. Gaddes, A. Hooper, and F. Albino. Simultaneous Classification and Location of Volcanic Deformation in SAR Interferograms Using a Convolutional Neural Network. *Earth and Space Science*, 11(6):e2024EA003679, June 2024. ISSN 2333-5084, 2333-5084. doi: 10.1029/2024EA003679. URL <https://agupubs.onlinelibrary.wiley.com/doi/10.1029/2024EA003679>.
- Ramon F Hanssen. *Radar interferometry: data interpretation and error analysis*, volume 2. Springer Science & Business Media, 2001.
- Kaiming He, Xiangyu Zhang, Shaoqing Ren, and Jian Sun. Deep residual learning for image recognition. *Proceedings of the IEEE conference on computer vision and pattern recognition*, pages 770–778, 2016.
- Hans Hersbach, Bill Bell, Paul Berrisford, Shoji Hirahara, András Horányi, Joaquín Muñoz-Sabater, Julien Nicolas, Carole Peubey, Raluca Radu, Dinand Schepers, et al. The era5 global reanalysis. *Quarterly journal of the royal meteorological society*, 146(730):1999–2049, 2020.
- Andrew Howard, Mark Sandler, Grace Chu, Liang-Chieh Chen, Bo Chen, Mingxing Tan, Weijun Wang, Yukun Zhu, Ruoming Pang, Vijay Vasudevan, Quoc V. Le, and Hartwig Adam. Searching for mobilenetv3. In *Proceedings of the IEEE/CVF International Conference on Computer Vision (ICCV)*, October 2019.
- MOGI Kiyoo. Relations between the eruptions of various volcanoes and the deformations of the ground surfaces around them. *Earthq Res Inst*, 36(99):e134, 1958.
- Spyros Kondylatos, Nikolaos Ioannis Bountos, Ioannis Prapas, Angelos Zavras, Gustau Camps-Valls, and Ioannis Papoutsis. Probabilistic machine learning for noisy labels in earth observation. *arXiv preprint arXiv:2504.03478*, 2025.
- Alexandre Lacoste, Nils Lehmann, Pau Rodriguez, Evan Sherwin, Hannah Kerner, Björn Lütjens, Jeremy Irvin, David Dao, Hamed Alemohammad, Alexandre Drouin, et al. Geo-bench: Toward foundation models for earth monitoring. *Advances in Neural Information Processing Systems*, 36:51080–51093, 2023.
- Milan Lazecký, Karsten Spaans, Pablo J González, Yasser Maghsoudi, Yu Morishita, Fabien Albino, John Elliott, Nicholas Greenall, Emma Hatton, Andrew Hooper, et al. Licsar: An automatic insar tool for measuring and monitoring tectonic and volcanic activity. *Remote Sensing*, 12(15):2430, 2020.
- Tsung-Yi Lin, Priya Goyal, Ross Girshick, Kaiming He, and Piotr Dollár. Focal loss for dense object detection. In *Proceedings of the IEEE international conference on computer vision*, pages 2980–2988, 2017.
- Zhuang Liu, Hanzi Mao, Chao-Yuan Wu, Christoph Feichtenhofer, Trevor Darrell, and Saining Xie. A convnet for the 2020s. *Proceedings of the IEEE/CVF Conference on Computer Vision and Pattern Recognition*, pages 11976–11986, 2022.
- Ilya Loshchilov and Frank Hutter. Decoupled weight decay regularization. *arXiv preprint arXiv:1711.05101*, 2017.

- Susan C Loughlin, Robert Stephen John Sparks, Steve Sparks, Sarah K Brown, Susanna F Jenkins, and Charlotte Vye-Brown. *Global volcanic hazards and risk*. Cambridge University Press, 2015.
- Didier Massonnet and Kurt L Feigl. Radar interferometry and its application to changes in the earth's surface. *Reviews of geophysics*, 36(4):441–500, 1998.
- Alistair Miles, John Kirkham, Martin Durant, James Bourbeau, Tarik Onalan, Joe Hamman, Zain Patel, shikharsg, Matthew Rocklin, Raphael dussin, Vincent Schut, Elliott Sales de Andrade, Ryan Abernathy, Charles Noyes, sbalmer, pyup.io bot, Tommy Tran, Stephan Saalfeld, Justin Swaney, and Anderson Banihirwe. zarr-developers/zarr-python: v2.4.0, 2020. URL <https://doi.org/10.5281/zenodo.3773450>.
- Yoshimitsu Okada. Surface deformation due to shear and tensile faults in a half-space. *Bulletin of the seismological society of America*, 75(4):1135–1154, 1985.
- Amy L. Parker, Juliet Biggs, Richard J. Walters, Susanna K. Ebmeier, Tim J. Wright, Nicholas A. Teanby, and Zhong Lu. Systematic assessment of atmospheric uncertainties for insar data at volcanic arcs using large-scale atmospheric models: Application to the cascade volcanoes, united states. *Remote Sensing of Environment*, 170:102–114, 2015. ISSN 0034-4257. doi: <https://doi.org/10.1016/j.rse.2015.09.003>. URL <https://www.sciencedirect.com/science/article/pii/S0034425715301267>.
- Michael P. Poland. *Remote Sensing of Volcano Deformation and Surface Change*, pages 173–203. Springer International Publishing, Cham, 2024. ISBN 978-3-031-59306-2. doi: 10.1007/978-3-031-59306-2_9. URL https://doi.org/10.1007/978-3-031-59306-2_9.
- Robert Gabriel Popescu, Nantheera Anantrasirichai, and Juliet Biggs. Anomaly detection for the identification of volcanic unrest in satellite imagery. In *2024 IEEE International Conference on Image Processing (ICIP)*, pages 2327–2333. IEEE, 2024.
- Olaf Ronneberger, Philipp Fischer, and Thomas Brox. U-net: Convolutional networks for biomedical image segmentation. *Medical Image Computing and Computer-Assisted Intervention–MICCAI 2015: 18th International Conference, Munich, Germany, October 5-9, 2015, Proceedings, Part III 18*, pages 234–241, 2015.
- Maria Sdraka, Alkinoos Dimakos, Alexandros Malounis, Zisoula Ntasiou, Konstantinos Karantzas, Dimitrios Michail, and Ioannis Papoutsis. Floga: A machine learning ready dataset, a benchmark and a novel deep learning model for burnt area mapping with sentinel-2. *IEEE Journal of Selected Topics in Applied Earth Observations and Remote Sensing*, 2024.
- M. Shirzaei and R. Bürgmann. Topography correlated atmospheric delay correction in radar interferometry using wavelet transforms. *Geophysical Research Letters*, 39(1), 2012. doi: <https://doi.org/10.1029/2011GL049971>. URL <https://agupubs.onlinelibrary.wiley.com/doi/abs/10.1029/2011GL049971>.
- Freysteinn Sigmundsson, Sigrún Hreinsdóttir, Andrew Hooper, Thóra Arnadóttir, Rikke Pedersen, Matthew J Roberts, Níels Óskarsson, Amandine Auriac, Judicael Decriem, Páll Einarsson, et al. Intrusion triggering of the 2010 eyjafjallajökull explosive eruption. *Nature*, 468(7322):426–430, 2010.
- Karsten Spaans and Andrew Hooper. Insar processing for volcano monitoring and other near-real time applications. *Journal of Geophysical Research: Solid Earth*, 121(4):2947–2960, 2016.
- Gencer Sumbul, Arne De Wall, Tristan Kreuziger, Filipe Marcelino, Hugo Costa, Pedro Benevides, Mario Caetano, Begüm Demir, and Volker Markl. Bigearthnet-mm: A large-scale, multimodal, multilabel benchmark archive for remote sensing image classification and retrieval [software and data sets]. *IEEE Geoscience and Remote Sensing Magazine*, 9(3):174–180, 2021.
- Jian Sun, Christelle Wauthier, Kirsten Stephens, Melissa Gervais, Guido Cervone, Peter La Femina, and Machel Higgins. Automatic detection of volcanic surface deformation using deep learning. *Journal of Geophysical Research: Solid Earth*, 125(9):e2020JB019840, 2020.
- Mingxing Tan and Quoc Le. Efficientnetv2: Smaller models and faster training. In Marina Meila and Tong Zhang, editors, *Proceedings of the 38th International Conference on Machine Learning*, volume 139 of *Proceedings of Machine Learning Research*, pages 10096–10106. PMLR, 18–24 Jul 2021. URL <https://proceedings.mlr.press/v139/tan21a.html>.
- R. I. Tilling. The critical role of volcano monitoring in risk reduction. *Advances in Geosciences*, 14:3–11, 2008. doi: 10.5194/adgeo-14-3-2008. URL <https://adgeo.copernicus.org/articles/14/3/2008/>.
- Sébastien Valade, Andreas Ley, Francesco Massimetti, Olivier D'Hondt, Marco Laiolo, Diego Coppola, David Loibl, Olaf Hellwich, and Thomas R Walter. Towards global volcano monitoring using multisensor sentinel missions and artificial intelligence: The mounts monitoring system. *Remote Sensing*, 11(13):1528, 2019.

- Enze Xie, Wenhai Wang, Zhiding Yu, Anima Anandkumar, Jose M Alvarez, and Ping Luo. Segformer: Simple and efficient design for semantic segmentation with transformers. *Advances in neural information processing systems*, 34:12077–12090, 2021.
- Xue-Min Yang, Paul M Davis, and James H Dieterich. Deformation from inflation of a dipping finite prolate spheroid in an elastic half-space as a model for volcanic stressing. *Journal of Geophysical Research: Solid Earth*, 93(B5):4249–4257, 1988.
- Chen Yu, Zhenhong Li, and Nigel T Penna. Interferometric synthetic aperture radar atmospheric correction using a gps-based iterative tropospheric decomposition model. *Remote Sensing of Environment*, 204:109–121, 2018a.
- Zhiding Yu, Weiyang Liu, Yang Zou, Chen Feng, Srikumar Ramalingam, BVK Kumar, and Jan Kautz. Simultaneous edge alignment and learning. In *Proceedings of the European conference on computer vision (ECCV)*, pages 388–404, 2018b.
- Howard A Zebker, Paul A Rosen, and Scott Hensley. Atmospheric effects in interferometric synthetic aperture radar surface deformation and topographic maps. *Journal of geophysical research: solid earth*, 102(B4):7547–7563, 1997.
- Xiao Xiang Zhu, Sina Montazeri, Mohsin Ali, Yuansheng Hua, Yuanyuan Wang, Lichao Mou, Yilei Shi, Feng Xu, and Richard Bamler. Deep learning meets sar: Concepts, models, pitfalls, and perspectives. *IEEE Geoscience and Remote Sensing Magazine*, 9(4):143–172, 2021. doi: 10.1109/MGRS.2020.3046356.

Table 5: Overview of Hephaestus Minicubes Dataset Variables

Variable	Description
InSAR Products	
Phase Difference	Difference in SAR signal phase, indicating surface displacement.
Coherence	The reliability of the interferometric phase measurement.
Topography	
DEM	Digital Elevation Model: a representation of Earth’s surface topography.
Atmospheric Variables	
Total Column Water Vapour	Water vapour from surface to the top of the atmosphere.
Surface Pressure	Atmospheric pressure at Earth’s surface.
Vertical Integral of Temperature	Mass-weighted temperature integral from surface to top of the atmosphere.
Annotations	
Deformation Mask	High level mask for deformation presence {Non-Deformation, Volcanic, Earthquake}.
Activity Type Mask	Mask identifying the activity type: {Sill, Dyke, Mogi, Spheroid, Earthquake, Unidentified}.
Intensity Level Mask	Mask identifying the intensity level of the activity {None, Low, Medium, High}.
Phase	Phase of the activity: {Rest, Unrest, Rebound, None}.
Atmospheric Fringes	Identifies types of atmospheric noise.
Glacier Fringes	Identifies deformation patterns from glacier melting.
Orbital Fringes	Identifies phase ramps due to orbital errors.
Corrupted	Flag for corrupted data.
No Info	Identifies low-coherence interferograms, where meaningful interpretation is not possible.
Low Coherence	Identifies samples that are characterized from interferometric signal decorrelation.
Is Crowd	Identifies whether multiple deformation masks exist.
Caption	Expert text description of the interferogram and annotation rationale.
Confidence	Value indicating the annotator’s confidence [0–1].
Metadata	
Unique Id	Unique identifier for each sample.
Valid Date Pair	Boolean flag for primary/secondary dates with existing InSAR products.

A Detailed Dataset Description

This section details the annotation schema used in *Hephaestus Minicubes*. Building upon the expert labels from the original *Hephaestus* dataset [Bountos et al., 2022c], annotations were adapted to a spatiotemporal format compatible with the datacube structure. A comprehensive view of the dataset variables can be seen in Tab. 5 and examples of different annotation types are shown in A.1. In the following paragraphs we will detail the key variables of *Hephaestus Minicubes*.

Activity. Activity-related segmentation masks lie at the core of the dataset’s annotation schema detailing the presence of deformation, its geophysical source and its intensity.

A high-level *Deformation Mask*, delineates Volcanic and Earthquake induced deformation patterns.

The *Activity Type Mask* captures more detailed geophysical context, distinguishing among several common deformation source models: Mogi [Kiyoo, 1958], Dyke [Okada, 1985, Sigmundsson et al., 2010], Sill [Fialko et al., 2001], and Spheroid [Yang et al., 1988], as well as deformation attributed to Earthquake events or labeled as Unidentified when no clear model can be observed.

The *Intensity Level Mask* categorizes the strength of deformation signals based on the number of visible fringes in the interferogram: Low (1 fringe), Medium (2–3 fringes), and High (more than 3 fringes). For earthquake-related events, the intensity is marked as None, reflecting their distinct deformation characteristics.

Additionally, we include a *Phase* categorical variable that captures the state of the volcano *i.e.* Rest (no sign of volcanic activity), Unrest (indicating uplift), or Rebound (indicating subsidence). Again, for Earthquake events, we set the phase to None.

Noise. A separate set of annotation variables aim to capture specific signal characteristics and noise patterns. These include: *glacier fringes*, when observed fringes result from glacier melting

(1 if present, 0 otherwise); *orbital fringes*, for phase ramps caused by satellite orbital errors; and *atmospheric fringes*, which take four values: type 0 (no atmospheric impact), type 1 (vertical stratification correlated with topography due to changes in the troposphere’s refractive index), type 2 (turbulent mixing and vapors caused by liquid or solid particles in the atmosphere), and type 3 (a combination of type 1 and type 2). The *low coherence* variable is set to 1 when interferometric signal decorrelation dominates the image. *No info* is used when coherence is so low throughout the interferogram that meaningful interpretation is not possible.

InSAR Processing Errors. Automated InSAR generation pipelines may, occasionally, result in faulty products. To identify corrupted InSAR, and facilitate automatic detection of such instances in future applications, we include a set of annotation variables denoting technical faults. The first is the binary variable *corrupted*, which identifies interferograms that are entirely problematic and unusable. The second is *processing error*, which distinguishes between specific InSAR processing errors: type 1 refers to debursting errors during the synchronization of bursts from one or more sub-swaths; type 2 indicates Sentinel-1 sub-swath merging errors, which appear as visible discontinuities, while type 0 denotes interferograms free of such processing issues.

Meta-Information. The *confidence* score is a continuous value in the range $[0, 1]$ that reflects the annotator’s confidence regarding the deformation classification. The *is crowd* variable is set to 0 when at most one local fringe pattern is present and 1 when two or more such patterns appear within the same interferogram. Furthermore, the *caption* field contains a text description providing expert commentary, interpretation rationale, or relevant contextual notes for the InSAR phase difference product. Finally the *unique id* serves as a unique identifier for each sample, and the *valid date pair* flag indicates whether the combination of primary and secondary dates corresponds to an existing InSAR product, intended for use in the multi-dimensional array functionality.

Annotation Process. The annotation process was carried out by a team of InSAR experts through photo-interpretation on the available wrapped interferograms. Each image was optically inspected over the locations of volcanoes, as well as the surrounding areas, in order to evaluate the quality of the interferograms and indicate the impact of atmospheric delays and potential artifacts. Each positive annotation was cross-validated via external sources (publications, reliable news sources) as well as the COMET Volcano Deformation Portal ³, to support the evaluation of whether the observed displacement was due to true volcanic activity or atmospheric delay effects. For further details regarding the annotation process readers are referred to the original *Hephaestus* dataset [Bountos et al., 2022c].

A.1 Visualizing Annotation Diversity

In this section we present selected examples of different annotation variables, illustrating the diversity and richness of the annotation variables in *Hephaestus Minicubes*.

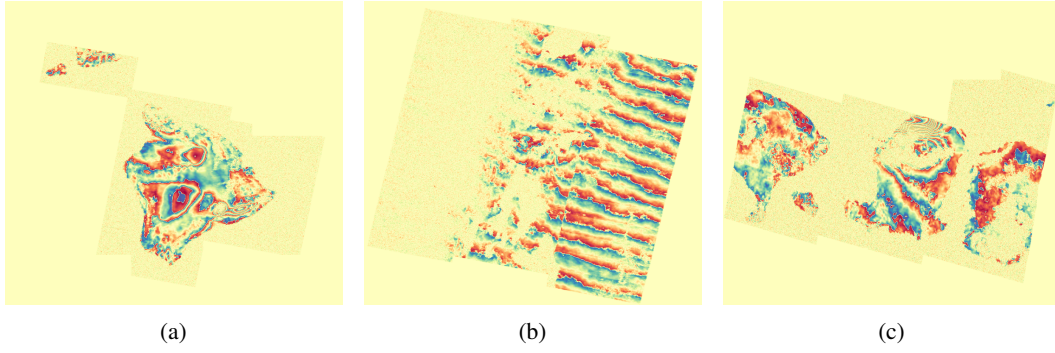
Text Captions. In Fig. 5, we showcase InSAR imagery with various apparent deformation patterns and atmospheric phenomena, together with the expert textual captions, highlighting the complexity and variability captured in the dataset. Each caption provides a thorough description of the location and type of all underlying phenomena, as well as a reference to interpretation challenges if present.

Activity and Intensity Masks. In Fig. 6, we present different time-series of InSAR products overlaid with expert-provided *activity type* and *intensity level* masks. These examples illustrate the temporal evolution of deformation signals and how distinct geophysical phenomena are annotated both categorically and in terms of intensity, emphasizing the structured labeling within *Hephaestus Minicubes*. The InSAR products are shown in grayscale for visual clarity.

B Extended Experimental Details

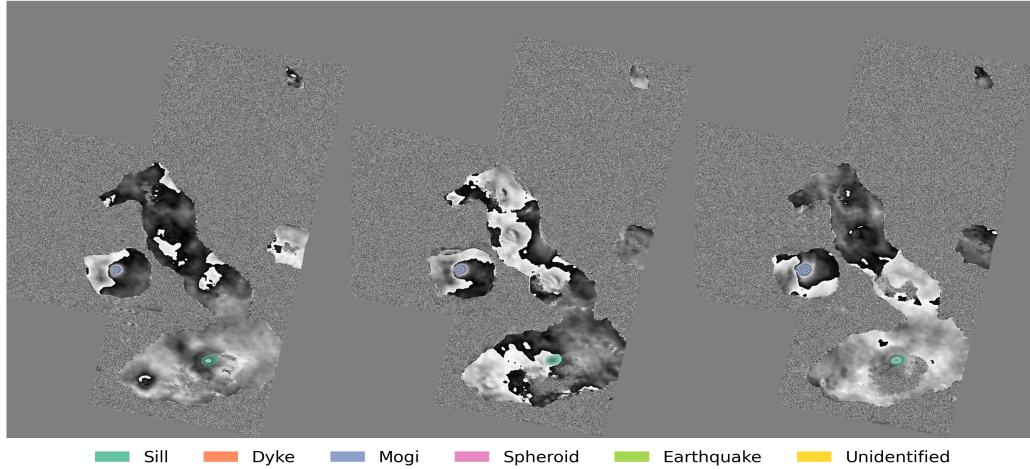
In this section we provide additional details on the experimental configurations used in the provided benchmark.

³<https://comet.nerc.ac.uk/comet-volcano-portal/>

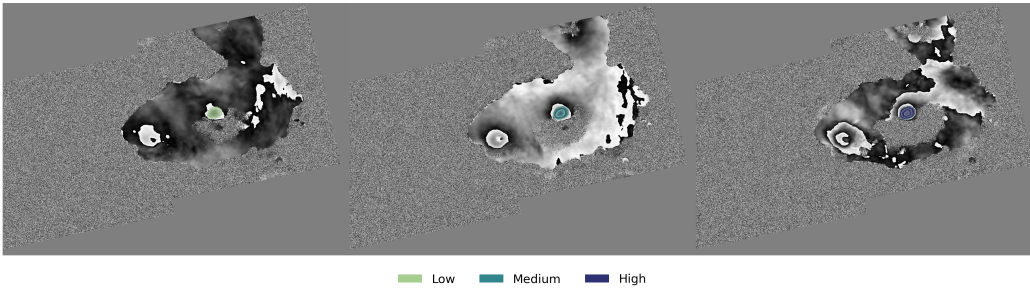


(a) "Vertical stratification can be detected on the high altitude areas. Turbulent mixing effect can also be detected on the right, central and top-left side. Two deformation patterns can be detected on the right side. A dyke-type of high intensity on the leftmost and sill-type of medium intensity on the rightmost. "
 (b) "Turbulent mixing effect or wave-like patterns caused by liquid and solid particles of the atmosphere can be detected around the area. No deformation activity can be detected. Orbital fringes detected. Difficulties in extracting information."
 (c) "Noise can be detected on the bottom-right area. Turbulent mixing effect can be detected on the wider left and central side of the region. Vertical stratification can also be detected on the central-top side of the region. An earthquake deformation pattern can be detected on the top-central side of the region."

Figure 5: Textual annotations highlighting volcanic and atmospheric phenomena in InSAR imagery from the *Hephaestus Minicubes* dataset.



(a) Overlay of *activity type* masks on a time-series of InSAR phase difference products.



(b) Overlay of *intensity level* masks on a time-series of InSAR phase difference products.

Figure 6: Examples of annotated InSAR products with overlaid annotated masks indicating: (a) distinct geophysical activity types and (b) activity intensity levels.

Time-series Construction. We construct the time-series by first grouping samples based on their primary SAR acquisition date. The distribution of the length of the resulting time-series can be seen in Fig. 7. Based on this, we fix the time-series length to 3, to ensure input consistency. For primary SAR acquisitions that produce time-series with length greater than 3, we extract all possible sub-sequences of the predefined length. Conversely, if they contain fewer than 3, we randomly duplicate available interferograms to reach the required time-series length.

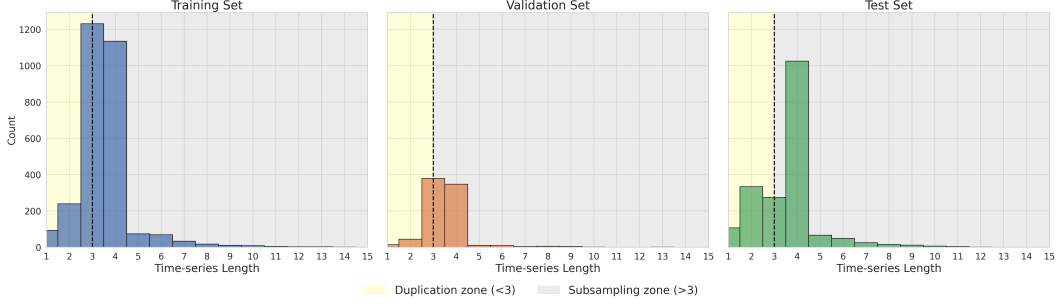


Figure 7: Distribution of time-series lengths across training, validation, and test sets.

Training Setup. We conducted all experiments on a single GPU (NVIDIA GeForce RTX 3090 Ti). We trained all models for 90 epochs, using the AdamW optimizer [Loshchilov and Hutter, 2017] with a fixed learning rate of 10^{-5} and a weight decay set to 10^{-2} . For classification, we found that cross-entropy loss consistently delivered the best performance, except for ViT that displayed more stable convergence with focal loss. For segmentation, focal loss was more effective, likely due to its robustness to class imbalance in pixel-wise annotations [Lin et al., 2017]. To mitigate the effect of class imbalance, we employed an undersampling strategy during training. For each epoch, all available positive samples were included, along with a randomly selected subset of negative samples of equal size. All models were trained with a random set of data augmentations including gaussian blur, random resize crop, horizontal and vertical flips and random rotations. Tables 6 and 7 report the number of trainable parameters for all models along with the average runtime of each experiment for both classification and segmentation tasks respectively.

Table 6: Overview of classification architectures

Model architecture	# Trainable parameters (M)		# Average runtime (hours)	
	Single-image	Time-series	Single-image	Time-series
ResNet-50	23.5	23.6	2.2	2.7
MobileNetV3 (Large)	4.2	4.2	1.7	2.0
EfficientNetV2 (Small)	20.2	20.2	2.6	2.7
ConvNeXt (Small)	87.6	87.6	4.9	5.4
ViT (Small)	22.3	24.0	2.5	3.2

Table 7: Overview of segmentation architectures

Model architecture	Backbone	# Trainable parameters (M)		# Average runtime (hours)	
		Single-image	Time-series	Single-image	Time-series
DeepLabV3	ResNet-50	26.7	26.8	2.3	2.9
UNet	ResNet-50	32.5	32.6	2.3	3.0
SegFormer	ResNet-50	24.9	24.9	1.6	3.7

C Qualitative Results and Model Insights

In this section, we present indicative examples that provide insights on models’ performance beyond quantitative metrics, especially given the inherent ambiguities and complexities of the data.

Ambiguity in Segmentation Masks. As discussed in section 5 of the main text, delineating the exact boundaries of deformation is often ambiguous, especially in regions of high-incoherence. Such

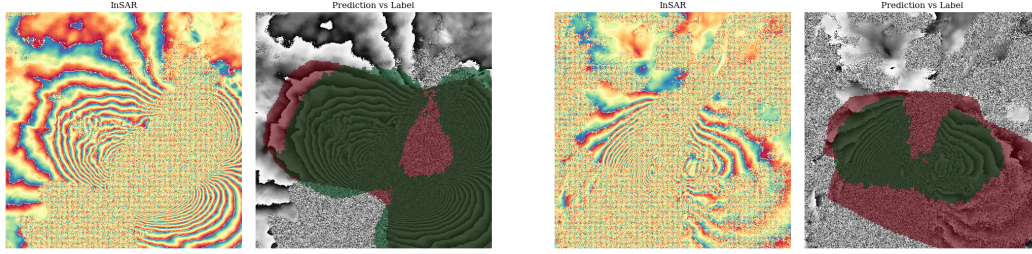
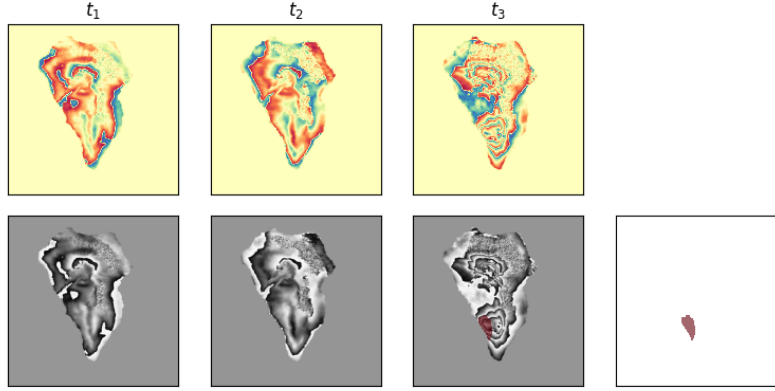


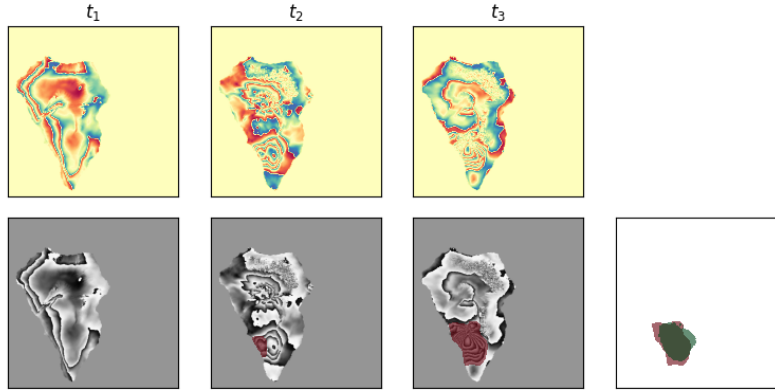
Figure 8: Qualitative examples of true positive model predictions that illustrate the inherent ambiguity in segmentation masks, where deformation extent is difficult to define. The left image of each pair depicts the InSAR phase difference, while the right image overlays the ground truth mask (in red) and the model prediction (in green) on the InSAR product (in grayscale). The results presented here have been obtained by the best performing DeepLabV3 model, which utilizes atmospheric data as input.

noise is inherent to the data itself, making the annotation, and thereby accurate prediction challenging. In Fig. 8 we offer two representative examples of qualitatively good model predictions that do not perfectly align with the annotator’s estimation, indicating the aforementioned ambiguity. In this case, model predictions accurately identify the observable deformation patterns to some extent, but exclude the noisy areas. The human annotator, however, includes these noisy regions, considering them as part of the event, even if they do not exhibit ground deformation fringes.

Time-Series Predictions. Fig. 9 illustrates important insights concerning model predictions on time-series inputs. Although both time-series of the figure focus on the same volcanic region, variations in the spatial extent or deformation onset across time-steps can affect detection ability. In the first sequence, less-pronounced deformation patterns are only visible in the final time-step, which the model fails to detect. In contrast, the second sequence displays a progressively intensifying deformation signal starting from the second time-step, providing stronger temporal cues that allow the model to correctly identify and segment the affected area. This example highlights how both the timing and strength of deformation signals across the time-series could play an important role in the the model’s ability to identify deformation.



(a)



(b)

Figure 9: Time-series examples over La Palma, Tenerife, demonstrating the role of temporal context in model predictions. The upper image series of each subfigure depicts the InSAR products in each timestep, and the lower image series depicts the ground truth masks (in red) for each time step with the corresponding InSAR in grayscale as the background. The last image in the lower series depicts the union of all ground truth masks (in red) and the model predictions (in green). Results have been obtained with the best performing SegFormer model (with atmospheric input). Subfigure a) shows a false negative case where only the final time-step exhibits deformation, which the model fails to detect, while subfigure b) illustrates a case where the model successfully identifies the deformation due to its increased presence in the last two time-steps. These examples highlight how variations in signal strength and onset time can influence model prediction.